


Time-dependent semiclassical scattering dynamics: Electronically elastic and charge-transfer study of $\text{H}^+ + \text{O}_2$ at keV collision energies

Deboki Reja  and Sanjay Kumar*

Department of Chemistry, *Indian Institute of Technology Madras*, Chennai 600036, India



(Received 10 June 2024; accepted 12 August 2024; published 3 September 2024)

The collision dynamics of H^+ with O_2 have been carried out at high collision energies $E_{\text{c.m.}} = 0.096\text{--}4.848$ keV ($E_{\text{lab}} = 0.1\text{--}5.0$ keV) within the time-dependent semiclassical straight line trajectory approach. For high collision energy, ions (projectiles) are expected to follow a straight line trajectory, and the collision time scales allow us to consider sudden approximations for the rovibrational motions. Therefore, the dynamical calculations have been performed using rigid-rotor potential-energy surfaces. The *ab initio* adiabatic potential-energy surfaces exhibit nonadiabatic interactions between the entrance and charge-transfer (CT) channels. Dynamical attributes such as differential cross sections and integral cross sections for the electronically elastic and the CT processes have been calculated using the quasidiabatic surfaces and potential couplings and have been compared with the available data from the scattering experiments.

DOI: [10.1103/PhysRevA.110.032802](https://doi.org/10.1103/PhysRevA.110.032802)

I. INTRODUCTION

The importance of ion- and atom-molecule collisions is well realized in areas of interstellar, upper planetary, and cometary atmosphere [1]. These collisions lead to three basic inelastic processes: (i) the excitation of either of the collision partners (vibrational or rotational excitations), (ii) the transfer of electrons between target and projectile [charge-transfer (CT)], and (iii) the ejection of electrons from the target or the projectile [2]. The CT or charge exchange (CE) is described as a process in which an ion takes one (single electron capture) or more (multielectron capture) electrons from another atom or molecule. The electron capture by the ions from the molecules present in the Earth's atmosphere and interstellar spaces has been observed on a large variety of objects, such as comets and planets in the interstellar media [3].

X-ray emissions from many comets have been observed, and their origin is interpreted due to charge transfer between the stellar or solar wind ions (H^+ , He^+) and small molecules (CO , N_2 , CO_2 , NO , and O_2) leading to various electronic states excitation [3,4]. The stream of ionized particles present in the stellar wind moves with a speed ranging from 20 km/s (cool stars) to 2000 km/s (hot, massive stars). The proton is the most abundant ion in the interstellar medium, and its kinetic energy (KE) is in the range of approximately 2.0 eV to 20 keV. The Sun is a medium-sized star, and the speed of the constituents of solar wind varies from 200 to 800 km/s. This is approximately equivalent to the energy range of 0.2–3.3 keV for the proton. Solar protons enter the Earth's upper atmosphere with kinetic energy in keV and lose most of their energy in the ionosphere, and interact with several diatomic and polyatomic molecules present in the stratosphere in the range of 0–100 eV. These interactions significantly affect the stratospheric dynamics. Interestingly, in the collision energy

range 0–30 eV, O_2 shows maximum vibrational excitation in its ground electronic state compared to other diatoms (CO , N_2 , NO) present in the stratosphere [5]. In fact, the vibrational excitations in these molecules remain very low; the higher vibrational excitations in O_2 have been explained due to the participation of the next higher electronic excited states [5–7]. Cross sections for processes occurring through the collision of H^+ with O_2 in keV range energy are vital, as they give insights into the chemistry of the upper planetary atmosphere and interstellar media. The present paper focuses on semiclassical dynamics studies on electronically elastic as well as CT processes leading to various electronic excited states of O_2^+ for the collision of H^+ with O_2 at the high collision energy ranges (\approx keV).

Measurements of differential cross sections (DCSs) for the $\text{H}^+ + \text{O}_2$ system in the forward scattering angle $0.02^\circ\text{--}1.0^\circ$ for the collision energies of 0.5, 1.5, and 5 keV in the laboratory frame have been measured by Gao *et al.* [8]. These experiments were carried out by them in a molecular beam scattering setup as described by Newman *et al.* [9]. The work was further extended by Cabrera-Trujillo *et al.* [10] for $\theta_{\text{lab}} = 0.15^\circ$ and 5° in the laboratory frame to measure the absolute differential and integral cross sections (ICSs) for the elastic and charge-transfer processes. The experimental setup adopted by them was similar to that of Gao *et al.* [8]. Total experimental cross sections at high collision energies have also been reported in the literature [8,11–16].

Cabrera-Trujillo *et al.* [10] reported theoretical calculations for elastic and CT processes for the collision energy in the range 0.5–25 keV using the electron-nuclear dynamics (END) model [17,18]. The wave functions of the ground electronic state of the $\text{H}^+ + \text{O}_2$ system were represented at the self-consistent level (SCF) level of accuracy using Dunning's contracted basis sets, O : $[6s3p/3s2p]$ and H : $[5s2p/5s2p]$ [19]. Their study showed that large impact parameter collisions had negligible contribution to the CT process. The measured DCS values showed a high value in the forward scattering, followed

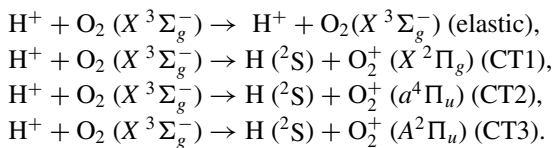
*Contact author: sanjay@iitm.ac.in

by a sharp decrease in the cross-section values for larger scattering angles. They also calculated ICSs and compared them with the earlier available data.

Dynamics studies of ion-molecule collisions require highly refined potential-energy surfaces (PESs). If the excited states are involved in the dynamics, one should carefully examine their involvement in influencing the overall dynamical outcomes at a collision energy. In such cases, dynamics need to be carried out on the electronic ground and several excited PESs. Computations of accurate PESs (both adiabatic and quasidiabatic PESs) on the $H^+ + O_2$ system have been carried out using various levels of theories [20–24]. Saheer and Kumar [25] presented the adiabatic and quasidiabatic potential-energy surfaces for the ground and the first three excited ($1-4\ ^3A''$) electronic states of the system in the Jacobi scattering coordinates.

Dynamics studies at low to moderate collision energy ranges (1–100 eV) on the $H^+ + O_2$ system have been reported in the literature [7,24,26]. Amaran and Kumar [7,24] performed quantum-mechanical calculations under the vibrational close-coupling rotational infinite-order approximation to study the vibrational excitation and CT dynamics at 9.5 and 23 eV on two-state coupled PESs computed using multireference configuration interaction (MRCI) level of theory and cc-pVTZ basis set. The results were found to be in good agreement with those of experiments [27], suggesting the adequacy of the quasidiabatic PESs and quasidiabatization using the *ab initio* procedure [28].

It is important to note that, at high energy (\approx keV), the higher electronic states become energetically accessible. The combined experimental and theoretical studies by Cabrera-Trujillo *et al.* [10] and Gao *et al.* [8] could provide information only on the total CT cross section, and information on the state-resolved CT channels could not be obtained. In our earlier studies on the construction of *ab initio* PESs at the MRCI level of accuracy and cc-pVTZ basis set [25], the following four lowest electronic states have been identified to yield the electronically elastic (sometimes also referred to as “direct”) and CT processes:



To the best of our knowledge, an elaborate state-selective study at high collision energy for these processes is still lacking. Therefore, in the present paper, we have performed the collision dynamics for the electronically elastic and state-selective CT processes within the semiclassical time-dependent straight line trajectory approach for the collision energies $E_{c.m.} = 0.096\text{--}4.848$ keV. The present paper would also be a benchmark to test the accuracy of the PESs and the *ab initio* diabaticization procedure for high-energy dynamics calculations.

The paper is arranged as follows: The theoretical formulations for the essential semiclassical time-dependent straight line trajectory approach are given in Sec. II. Details on the *ab initio* PESs and the corresponding radial couplings among them are presented in Sec. III. Computational details of the

collision dynamics, calculations of collision parameters, and dynamical attributes are given in Sec. IV. A summary with the conclusion is given in Sec. V.

II. SEMICLASSICAL TIME-DEPENDENT STRAIGHT LINE TRAJECTORY METHOD

A full quantum-mechanical treatment of a computationally tractable collision system considering all degrees of freedom would yield exact results. In the keV collision energy range, a large number of channels (electronic, vibrational, and rotational) become energetically accessible, and the calculations become increasingly prohibitive computationally. Therefore, in practice, one can invoke approximations which could be physically valid to carry out scattering dynamics. The infinite-order-sudden approximation is one such approximation where the rotational motions of the diatom are considered frozen, and the energy spacing between the rotational states is ignored in view of high collision energy. The time period for the rotational and vibrational motions of the diatom are of the order of pico- and femtoseconds, respectively. At the higher energies (\approx keV), the collision time (10^{-18} s) is approximately six and three orders of magnitudes less compared to a typical rotational and a vibrational motion of the diatom, respectively. This allows one to carry out collision dynamics within the semiclassical framework, wherein vibrational and electronic degrees of freedom are treated quantum mechanically, and the translational and rotational motions are treated classically. In fact, the relative motion of the colliding partners can be approximated to follow a straight line trajectory, and the rotation of the diatom can be considered as frozen. In such cases, the time-dependent Schrödinger equation is solved for a particular trajectory and further for a large number of trajectories. The results are finally averaged out to obtain the cross sections. The semiclassical trajectory method has been formulated and well documented in the literature [29–31] and references therein. For convenience, we provide the relevant descriptions and details below. For a collision pair, ($A + BC$), in Fig. 1, where A denotes an ion or atom colliding with diatom BC , one can treat the dynamics in the Jacobi scattering coordinates, where R is the vector joining A to the center of mass (c.m.) of BC , r defines the B - C vector, and γ defines the angle between them. The relative motion of the colliding partners can be approximated to follow a straight line trajectory, $R(t) = b + vt$, as shown in Fig. 1. In the straight line trajectory model, b is the impact parameter vector perpendicular to the incident velocity v . θ_r and ϕ_r define the molecule's orientations. ϕ_r and ϕ_b are the azimuthal angles related to the impact parameter, b . $\psi = \phi_b - \phi_r$ is physically significant as the whole system is invariant with respect to the rotation of the diatom. The two most important relations used in this coordinate system are

$$\begin{aligned} R(t) &= \sqrt{b^2 + v^2 t^2}, \\ \cos \gamma &= (b \sin \theta_r \cos \psi + vt \cos \theta_r)/R(t). \end{aligned} \quad (1)$$

One can solve for the internal motion of the diatom along the internal coordinate (r) quantum mechanically in the time-dependent potential field of external coordinates (R), which are constrained to follow a straight line trajectory ($R(t)$).

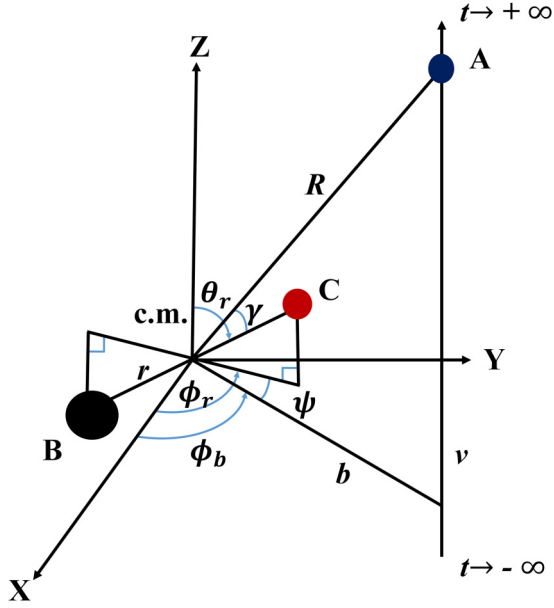


FIG. 1. Collision geometry for the $A + BC$ scattering in the impact parameter model. R , r , and γ define the Jacobi scattering coordinates. b , ψ , θ_r , and ϕ_r describe the trajectory. b and v are perpendicular to each other. For details, see the text. Adopted from Ref. [32].

The total Hamiltonian for the nonreactive $A + BC$ molecular scattering system in the Jacobi scattering coordinates (as defined in Fig. 1) can be written as

$$\hat{H}_{\text{tot}}(r, R, \gamma) = -\frac{\hbar^2}{2\mu_{A,BC}} \nabla_R^2 + \hat{H}_{BC}(r) + V^I(r, R, \gamma) + \hat{H}^e(q, r, R, \gamma) \quad (2)$$

where $-\frac{\hbar^2}{2\mu_{A,BC}} \nabla_R^2$ is the KE operator for the relative motion, \hat{H}_{BC} is the total Hamiltonian of diatom BC , and $H^e(q, r, R, \gamma)$ is the electronic Hamiltonian. q stands for the electronic coordinates. $\mu_{A,BC}$ is the reduced mass of the atom-ion-diatom system ($\mu_{A,BC} = \frac{(m_B + m_C)m_A}{(m_B + m_C) + m_A}$). $V^I(r, R, \gamma) [= V(r, R, \gamma) - V(r, R \rightarrow \infty, \gamma)]$ is the interaction potential of the atom or ion with the diatom, with $V^I(r, R, \gamma) \rightarrow 0$ as $R \rightarrow \infty$. $\hat{H}_{BC}(r) = \hat{h}_{\text{vib}}(r) + \hat{h}_{\text{rot}}(r)$, where $\hat{h}_{\text{vib}}(r)$ and $\hat{h}_{\text{rot}}(r)$ stand for the vibrational and rotational energies of the diatom (BC), respectively.

Under the approximation that A follows a straight line trajectory, the total Hamiltonian can be decoupled as

$$\hat{H}_{\text{tot}}(r, R, \gamma) = \hat{H}_A + \hat{H}_{\text{int}}(r, R, \gamma) \quad (3)$$

where $\hat{H}_{\text{int}}(r, R, \gamma)$ is the effective Hamiltonian

$$\hat{H}_{\text{int}}(r, R, \gamma) = \hat{H}_{BC}(r) + V^I(r, R(t), \gamma) + \hat{H}^e(q, r, R(t), \gamma) \quad (4)$$

and $\hat{H}_A = -\frac{\hbar^2}{2\mu_{A,BC}} \nabla_R^2$ yields the straight line trajectory. The rotational motion of the molecule can be treated in the sudden limit considering the collision time scale. Applying these

approximations, the effective Hamiltonian can be rewritten as

$$\hat{H}_{\text{int}}(r, R, \gamma) = \hat{h}_{\text{vib}}(r) + V^I(r, R(t), \gamma) + \hat{H}^e(q, r, R(t), \gamma). \quad (5)$$

The time-dependent Schrödinger equation for the collision pair ($A + BC$) in such framework is expressed as [33]

$$\hat{H}_{\text{int}}(r, R, \gamma) \Psi(r, R(t), \gamma) = i\hbar \frac{\partial}{\partial t} \Psi(r, R(t), \gamma). \quad (6)$$

The wave function $\Psi(r, R(t), \gamma)$ is expanded as

$$\Psi(r, R(t), \gamma) = \sum_{n,v} a_{n,v}(R(t)) \Phi_n(q_i; r, R(t), \gamma) \times \chi_{n,v}(r; R(t), \gamma) \quad (7)$$

where n, v are the electronic and vibrational states. Φ_n and $\chi_{n,v}$ are the electronic and the vibrational wave functions, respectively. The expansion coefficients, $a_{n,v}$ (complex in nature), contain comprehensive information about the dynamical features and depend on time via the straight line trajectory $R(t)$ of A . The electronic Hamiltonian can be expressed as

$$\hat{H}^e \Phi_n(q_i; r, R(t), \gamma) = E_n(r, R(t), \gamma) \Phi_n(q_i; r, R(t), \gamma) \quad (8)$$

where E_n is the electronic energy.

The present paper focuses on the dynamic study of high-energy collisions (0.1–5.0 keV). In such cases, the collision time scale is in attoseconds, whereas the time scale of a typical vibrational excitation of a diatom is of the order of few subfemtoseconds. In such a scenario, the vibrational component of the diatom can be approximated to remain fixed, and one can apply the vibrational sudden approximation [34,35]. Therefore, calculations are carried out for fixed value r , that is, $r = r_e$, the equilibrium bond distance of the diatom, assuming that the diatom is in its ground electronic and ground vibrational state ($v = 0$). Under such approximation, substituting Eq. (7) in Eq. (6) and multiplying by $\Phi_n^*(q)$, followed by integrating over electronic coordinates q , we obtained the close-coupled equations (hereafter, in the atomic units, $\hbar = 1$)

$$i \frac{\partial a_n(t)}{\partial t} = \sum_{n' \neq n} a_{n'}(t) V_{nn'} \exp[-i(E_{n'} - E_n)t]. \quad (9)$$

Under this condition, the electronic coupling is evaluated with $r = r_e$, that is, $\langle \Phi_n(q) | V^I(r_e, R, \gamma) | \Phi_{n'}(q) \rangle = V_{n,n'}(r_e, R)$. Potentials are in the quasidiabatic framework.

Applying the boundary conditions below, the a_n 's are related to the scattering matrix (S_n) as

$$|S_n[R(b, r_e, t)]|^2 = |a_n[R(b, r_e, t \rightarrow +\infty)]|^2. \quad (10)$$

The scattering amplitude in terms of S -matrix elements for the small-angle scattering [36,37] within semiclassical approximations [38,39] is given as

$$f_{n',n}(\theta_r, \phi_r) = \frac{-ik}{2\pi} \int_{b=0}^{\infty} \int_{\psi=0}^{2\pi} \exp[-2ikb \sin(\theta_{\text{scat}}/2) \times \cos(\phi_r - \psi)] (S_{n',n} - \delta_{n',n}) b db d\psi. \quad (11)$$

The final scattering amplitude depends upon b and ψ , and can be calculated for a fixed molecular orientation, (θ_r, ϕ_r) . Averaging over the molecular orientations (θ_r, ϕ_r) finally gives

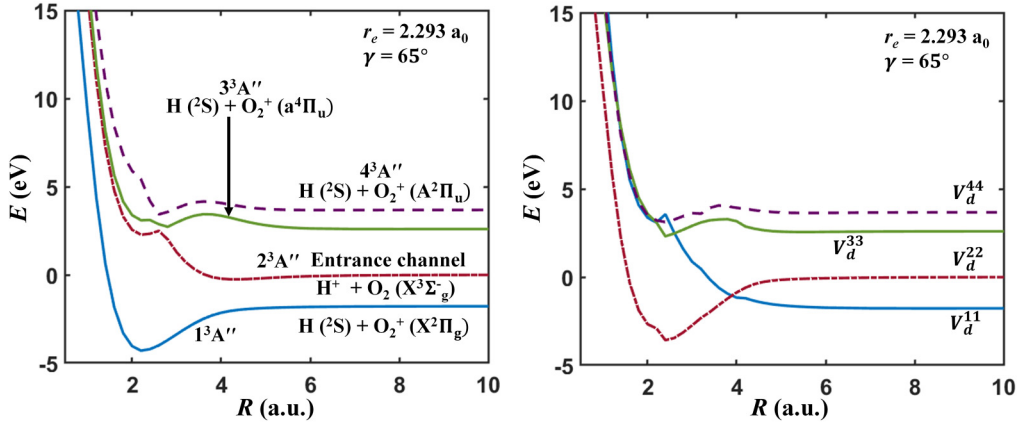


FIG. 2. *Ab initio* adiabatic (left panel) and corresponding quasidiabatic (right panel) PECs for the four lowest electronic states (1–4 $^3A''$) of the $H^+ + O_2$ system as a function of R for $\gamma = 65^\circ$, and $r = r_e = 2.293$ a.u. See the text for details.

us the differential cross sections for the electronic transition, $n \rightarrow n'$ [38]:

$$d\sigma_{n',n}(\theta_{\text{scat}}) = \frac{1}{4\pi} \int_{\theta_r=0}^{\pi} \int_{\phi_r=0}^{2\pi} |f_{n',n}(\theta_r, \phi_r)|^2 \sin \theta_r d\theta_r d\phi_r. \quad (12)$$

The knowledge of S_n -matrix elements can be applied further for the calculation of integral cross sections. The total state-to-state integral cross sections can be obtained as

$$\sigma_{n',n}(E_{\text{coll}}) = \frac{1}{2} \int_{\theta_r=0}^{\pi} \int_{b=0}^{\infty} \int_{\psi=0}^{2\pi} |(S'_{n',n} - \delta_{n',n})|^2 \times d\psi db d\theta_r. \quad (13)$$

III. AB INITIO PES AND COUPLINGS

In the present paper, we have used the available quasidiabatic PES points and the coupling potentials computed in our group [25] in the Jacobi scattering coordinates for the lowest four electronic states on the following grid points: $R = 1.8$ – 7 (0.2) and 8 – 15 (1.0); $r = 1.5$ – 3.5 (0.1); $\gamma = 0^\circ$ – 90° (7.5°). The data points for the *ab initio* adiabatic and quasidiabatic PESs, as well as the coupling potentials, are provided in the Supplemental Material [40]. As discussed in the previous section, the dynamics study for high-energy collisions can be carried out at the rovibrational sudden approximation. Therefore, the present dynamical study has been carried out using rigid-rotor PESs, that is, at $r = r_e = 2.293$ a.u., the equilibrium bond length of the diatom, O_2 . Before presenting the dynamics results, it would be worthwhile to discuss briefly the characteristics of the surfaces and the nonadiabatic couplings among them.

For the $H^+ + O_2$ system, the ground electronic state ($1^3A''$) asymptotically correlates to the charge-transfer channel, $H(^2S) + O_2^+(X^2\Pi_g^-)$, and the first excited state ($2^3A''$) correlates to the entrance channel, $H^+ + O_2(X^3\Sigma_g^-)$. The second ($3^3A''$) and third ($4^3A''$) excited states correlate to the $H(^2S) + O_2^+(a^4\Pi_u)$ and $H(^2S) + O_2^+(A^2\Pi_u)$, respectively. For the collinear ($\gamma = 0^\circ$) and perpendicular ($\gamma = 90^\circ$) approaches, there is direct curve crossing between $1^3\Sigma^-/1^3B_1$

and $1^3\Pi/1^3A_2$ as there is no radial coupling between them. But these direct crossings become avoided crossings for the off-collinear approaches. The degeneracy in the Π state is lifted into the A' and the A'' states. For an illustration, fresh sets of calculations have been performed, and the adiabatic PECs at $\gamma = 65^\circ$ and $r = r_e = 2.293$ a.u. as a function of R are shown in the left panel of Fig. 2 (computed using the MOLPRO suite of programs [41]). The adiabatic ground potential-energy curve (PEC) ($1^3A''$) and the first excited PEC ($2^3A''$) exhibit nonadiabatic interactions around $R = 4.5$ a.u. Similarly, $2^3A''$ and $3^3A''$, and $3^3A''$ and $4^3A''$, show avoided crossing at $R = 3.0$ and 3.2 a.u., respectively. The details of the quasidiabatization procedure have been given in our earlier paper [25]. Here, in Fig. 2 (right panel), we show the corresponding quasidiabatic potential (V_d). The entrance channel (V_{22}^d) shows curve crossing with the CT channels, V_{11}^d , V_{33}^d , and V_{44}^d at $R = 4.0$, 3.2 , and 3.0 a.u., respectively.

For the first-order nonadiabatic coupling matrix elements (NACMEs) ($\tau_{n',n}^1 = \langle \Phi_{n'}^a | \frac{\partial}{\partial R} | \Phi_n^a \rangle$), where Φ_n^a are electronic adiabatic wave functions, as mentioned above, we have undertaken a new set of calculations for $\gamma = 5^\circ$ and 85° to further examine the nonadiabatic interactions. For a meaningful discussion and convenience, we have used the data from our earlier calculations and shown the τ values in Fig. 3 for $\gamma = 15^\circ$ – 75° . Since the sign of the NACMEs is not uniquely defined [42,43], we have plotted their absolute values. First, we would like to focus on the interactions between the entrance and excited states (CT channels). τ_{12}^1 represents the coupling between the entrance and the CT1 channel. We observed sharp peaks for τ_{12}^1 at $\gamma = 5^\circ$ and 85° around $R = 4.5$ and 3.5 a.u., respectively, that is, for the near-collinear and near-perpendicular approaches, whereas a broad spread is noticed for τ_{12}^1 at $\gamma = 15^\circ$ – 75° , for the off-collinear approaches. This implies that nonadiabatic flux transfer will be more effective for the off-collinear approaches (τ_{12}^1 operates over a wider range of R) than for those collisions near the collinear geometries. Although τ_{12}^1 for the near collinear geometries are sharply peaked, they seem to be effective only over a limited range of R . This suggests that with the increase in the collision energy, the contributions from the near-collinear approaches will decrease since the projectile will have less time to spend

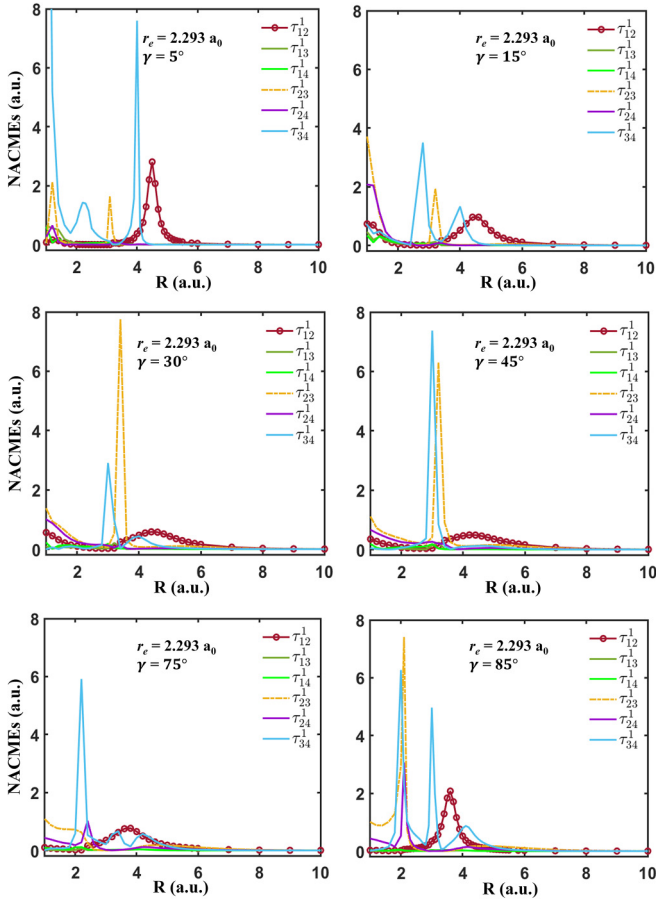


FIG. 3. Absolute NACME values ($\tau_{n',n}^1 = \langle \Phi_{n'}^a | \frac{\partial}{\partial R} | \Phi_n^a \rangle$) of the $\text{H}^+ + \text{O}_2$ system for off-collinear geometries ($\gamma = 5^\circ$ – 85°) as a function of R at $r_e = 2.293$ a.u. For details, see the text.

in the nonadiabatic interaction regions. The magnitudes of τ_{23}^1 and τ_{24}^1 , that is, the couplings between the entrance with the second and third CT channels, respectively, show sharp peaks and are effective only for $R = 2$ – 4 a.u. for all the orientations. This implies that CT excitations to these states will decrease with the increase in collision energies. Another way by which excited CT states can be populated is through indirect flux transfer from CT1 to CT2 and CT3. The magnitudes of τ_{13}^1 and τ_{14}^1 are much less as compared to the τ_{12}^1 . τ_{34}^1 exhibits multiple sharp peaks, more so for the near-collinear collisions, and therefore, it suggests that flux transfer from the CT2 to the CT3 channel will be effective. However, as discussed above, the flux transfer to the CT2 from the entrance channel is relatively weak as compared to that of the CT1. Therefore, contributions through such indirect flux transfers will be very small, and it is expected that at relatively low collision energies (relatively longer collision time), the probability of CT to the higher excited states will be higher as compared to that of higher collision energies (less collision time).

IV. SEMICLASSICAL DYNAMICS

A. Computational details

We provide here the essential computational details for the semiclassical time-dependent straight line trajectory

approach. The calculations are performed for $0^\circ \leq \phi_r \leq 360^\circ$, $0^\circ \leq \theta_r \leq 180^\circ$, $0^\circ \leq \psi \leq 360^\circ$, $1.0 \leq b \leq 8.0$ a.u. in the step size of 3.6° , 15° , 3.6° , and 0.07 a.u., respectively. The first-order coupled differential equations [Eq. (9)] are solved using the fourth-order Runge-Kutta method. The unitarity relation $\sum_n |a_n(t)|^2 = 1$ has been followed to test the numerical convergence with the initial condition, $a_1(t \rightarrow +\infty) = 1$. The time steps, $\Delta t = 0.03$ a.u. of time, were sufficient to get the convergence. The differential cross sections [Eq. (12)] are obtained from the scattering amplitudes [Eq. (11)] by averaging over the molecular orientations (ϕ_r, θ_r). The integral cross sections [Eq. (13)] are calculated by integrating over (θ_r, b, ψ) in the range of 0° – 360° (15°), 1.0 – 8.0 a.u. (0.07 a.u.), and 0° – 360° (3.6°), respectively (where numbers in the parentheses denote step sizes). Since all the theoretical calculations are performed in the c.m. frame, it will be appropriate to convert the available experimental data from the laboratory frame to the c.m. frame. The collision energy and scattering angle in the laboratory and c.m. frame are related as

$$E_{\text{c.m.}} = \frac{m_2}{m_1 + m_2} \times E_{\text{lab}}, \quad (14)$$

$$\sin \theta_{\text{c.m.}} = \frac{\sin \theta_{\text{lab}}}{m_2} \times (m_1 \times \cos \theta_{\text{lab}} + \sqrt{m_2^2 - m_2^2 \sin^2 \theta_{\text{lab}}}) \quad (15)$$

where c.m. and lab in subscript denote center-of-mass and laboratory frames, respectively. m_1 and m_2 are the masses of the projectile and target, respectively. Here, $m_1 = 1.0$ amu for the H atom and $m_2 = 32.0$ amu for the O_2 molecule.

B. Probability amplitude

Before we discuss the details on the cross sections, it would be helpful to have some insights into the dynamics in terms of the amplitudes of expansion coefficients ($|a_n(t)|^2$). We have studied the time dependence of the expansion coefficients as the collision proceeds for the energies $E_{\text{c.m.}} = 96.96, 484.85, 1454.55$, and 4848.48 eV. The corresponding values in the laboratory frame are $E_{\text{lab}} = 100, 500, 1500$, and 5000 eV, respectively. $R(t)$ defines the straight line trajectory of the projectile, and its range is chosen such that there is no further variation in the amplitude of $|a_n(t)|^2$, and the values reach the convergence limit. This range also varies depending on the chosen collision energy. To illustrate, the plots of $|a_n(t)|^2$ versus $R(t)$ (or t) for the electronically elastic channel— $n' = 0$, $[\text{H}^+ + \text{O}_2 (X^3\Sigma_g^-) \rightarrow \text{H}^+ + \text{O}_2 (X^3\Sigma_g^-)]$ —and the CT channels— $n' = 1$, CT1 $[\text{H}^+ + \text{O}_2 (X^3\Sigma_g^-) \rightarrow \text{H} (^2\text{S}) + \text{O}_2^+ (X^2\Pi_g)]$; $n' = 2$, CT2 $[\text{H}^+ + \text{O}_2 (X^3\Sigma_g^-) \rightarrow \text{H} (^2\text{S}) + \text{O}_2^+ (A^4\Pi_u)]$; $n' = 3$, CT3 $[\text{H}^+ + \text{O}_2 (X^3\Sigma_g^-) \rightarrow \text{H} (^2\text{S}) + \text{O}_2^+ (A^2\Pi_u)]$ —for two specific geometries— $\psi = 0^\circ$, $\theta_r = 30^\circ$, $b = 3.0$ and $\psi = 0^\circ$, $\theta_r = 60^\circ$, $b = 3.5$ a.u.—are shown in Fig. 4. We have magnified the magnitude of CT3 by 1.5 times for a better illustration. We choose the impact parameter values of $b = 3.0$ and 3.5 a.u., as the scattering matrix elements ($|S_n|^2$) for the CT1 are significant in magnitude in this range of b . The CT1 $[\text{H}^+ + \text{O}_2 (X^3\Sigma_g^-) \rightarrow \text{H} (^2\text{S}) + \text{O}_2^+ (X^2\Pi_g)]$ appears to be the dominant channel and also the most probable CT process for all the studied collision energies. At $E_{\text{c.m.}} = 96.96$ and 484.85 eV, the amplitude of $|a_n(t)|^2$ for $n' = 2$ and 3 [see Figs. 4(a)–4(d)] is higher as

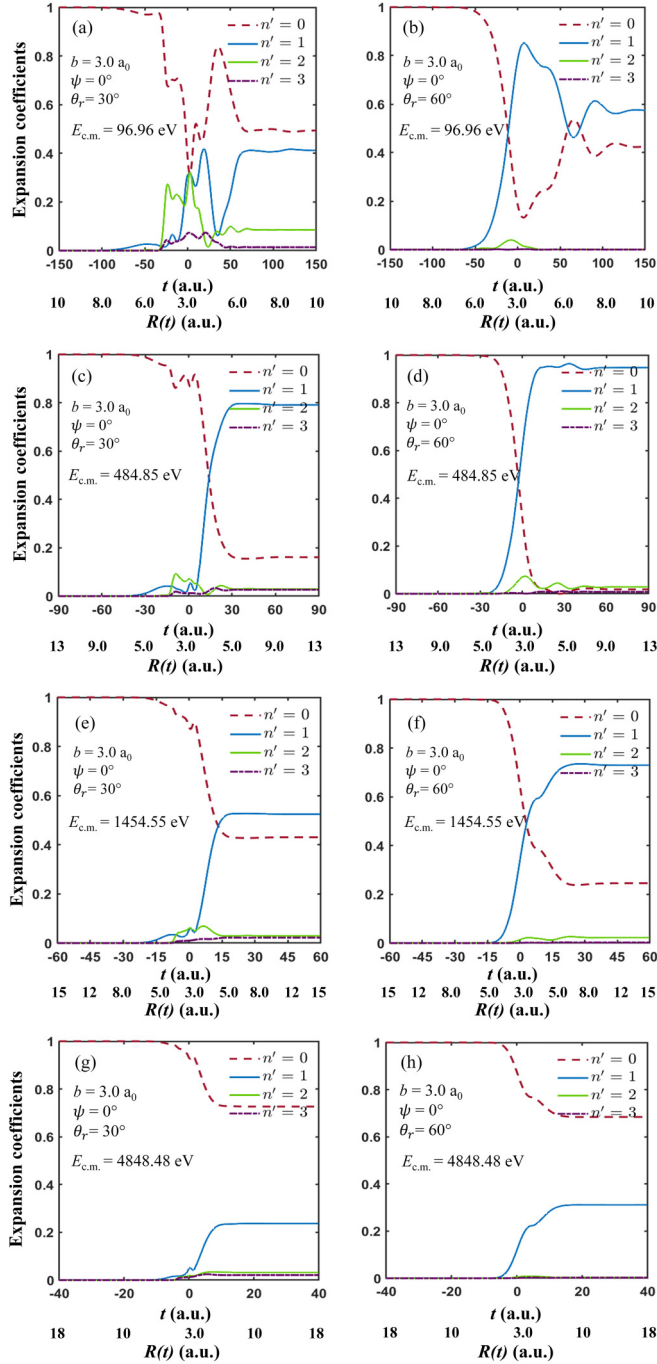


FIG. 4. Expansion coefficients $|a_n(t)|^2$ as a function of $R(t)$ for two different molecular orientations $\psi = 0^\circ$, $\theta_r = 30^\circ$, $b = 3.0$ a.u. and $\psi = 0^\circ$, $\theta_r = 60^\circ$, $b = 3.5$ a.u. at collision energies (a), (b) $E_{c.m.} = 96.96$ eV, (c), (d) 484.85 eV, (e), (f) 1454.55 eV, and (g), (h) 4848.48 eV. Electronically elastic, $n' = 0$ (brown lines); CT1, $n' = 1$ (blue lines); CT2, $n' = 2$ (green lines); CT3, $n' = 3$ (violet lines). For better clarity, the curves for $n' = 3$ have been multiplied by a factor of 1.5.

compared to those of high collision energies ($E_{c.m.} = 1454.55$ and 4848.48 eV) [see Figs. 4(e)–4(h)]. For an interaction domain of 20 a.u., the collision time for a projectile (here, H^+) with KE of 96.96 and 4848.48 eV is approximately of the order of 10^{-16} and 10^{-17} s, respectively. When the

velocity of the ion (H^+) is relatively less, it stays for a relatively longer time in the interaction zone, thus facilitating the charge-transfer processes leading to excitations to the CT2 and the CT3 channels, which is also in accordance with the strength and behavior of NACME values (τ^1) (discussed in Sec. III).

The above observation becomes more clear with the plot of S -matrix elements as a function of impact parameter b . The S matrix, $|S_n[R(b, r, t)]|^2 = |a_n[R(b, r, t \rightarrow +\infty)]|^2$ (computed after the completion of the collision) as a function of impact parameter b has been shown in Fig. 5 for two different orientations of θ_r at fixed ψ . Plots have been shown for the elastic ($n' = 0$) and CT channels ($n' = 1-3$) at $\psi = 0^\circ$, $\theta_r = 30^\circ$ and 60° , respectively. We observe that the amplitude of $|S_n[R(b, r, t)]|^2$ for $n' = 1$ is higher than those of $n' = 2$ and 3. Excitations to the CT1 are effective for b in the range of 1–6 a.u., which is again in conformity with the behavior of NACMEs (Fig. 3, τ_{12}^1 values show a broad spread up to $R = 6$ a.u.). The amplitudes of $|S_n|^2$ for $n' = 2$ and 3 are less effective largely for $b = 1-3$ a.u., since τ_{23}^1 , τ_{24}^1 , and τ_{34}^1 show sharp peaks for R values of 1–3 a.u. The amplitudes of $|S_n|^2$ for $n' = 2$ and 3, that is, CT to the O_2^+ ($a^4\Pi_u$) and O_2^+ ($A^2\Pi_u$), are observed to be higher in case of low collision energies than those of the high collision energies. The presence of oscillatory behavior in the S matrix, especially for the low collision energies and low impact parameter values, can be presumably explained in terms of relatively longer time duration of the ion in the interaction zone, where the flux transfers to the CT2 and CT3 occur along with the dominant CT1 from the entrance channel. With the increase in collision energy, the peaks become less pronounced and broader, affecting the flux transfer mostly to the CT1 state.

Let us now discuss the details of scattering amplitude $[f_{n',n}(\theta_r, \phi_r)]$. They exhibit rapid oscillations, pose a challenge for achieving numerical convergence, and become the computational bottleneck. The plot of $|f_{n',n}(\theta_r, \phi_r)|^2$ as a function of b at the experimental collision energies of 96.96 and 1454.55 eV are shown in Fig. 6 for the CT channels ($n' = 1-3$) for a particular orientation (specified in the Fig. 6). The amplitudes for the CT1 are higher than those of the CT2 and CT3 channels for both the collision energies. However, at $E_{c.m.} = 96.96$ eV, we observed that the scattering amplitudes for the higher excitations (CT2 and CT3) are relatively higher than those of higher collision energies, which can also be explained in accordance with the collision time scale as discussed above. At both collision energies, the amplitudes of scattering for the CT1 channel become negligibly small beyond 5.0 and 7.0 a.u., respectively. Calculations of $|f_{n',n}(\theta_r, \phi_r)|^2$ are further extended for the b values of 9.0, 10.0, and 12.0 a.u., and we observed almost negligible amplitude in this b range. Therefore, we can infer that the larger impact parameters (beyond $b = 8.0$ a.u.) do not contribute to the magnitude of $|f_{n',n}(\theta_r, \phi_r)|^2$. Similar behavior is observed in the work of Cabrera-Trujillo *et al.* [10].

C. Differential cross sections

Since differential cross sections contain the most important and valuable information about the interaction potential and the scattering processes, we have calculated DCSs using Eq. (12) for the electronically elastic channel [$H^+ + O_2$

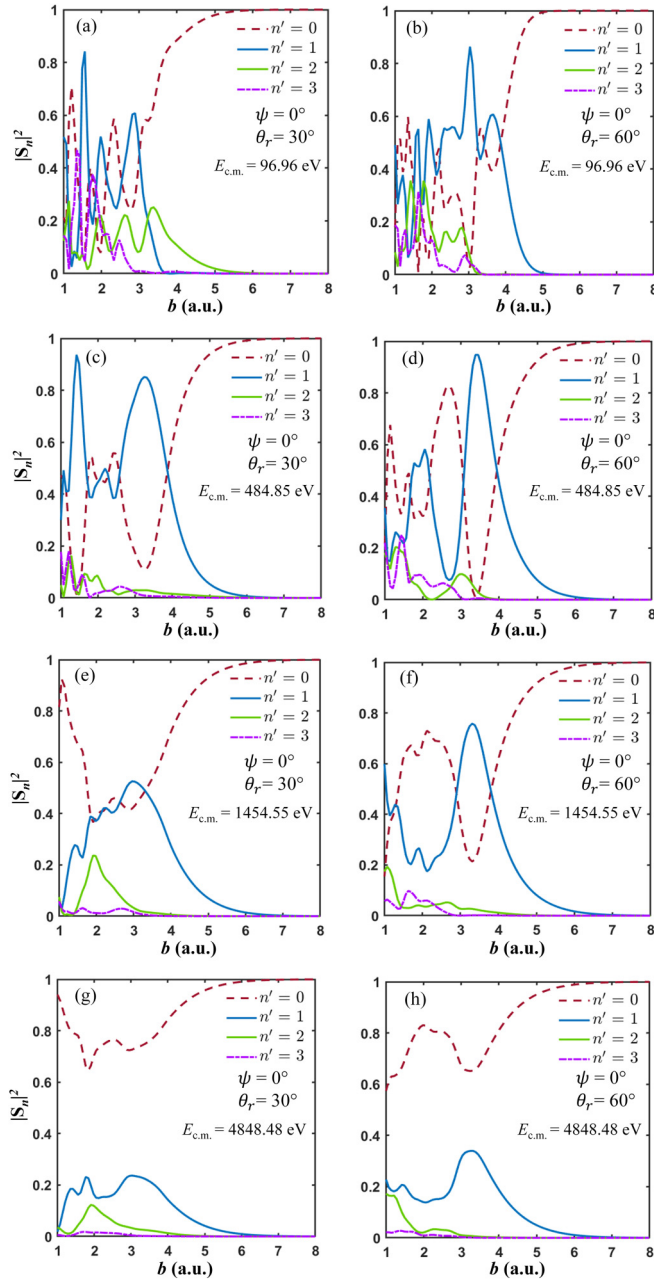


FIG. 5. The S -matrix elements $|S_n|^2$ as a function of impact parameter b for two different molecular orientations $\psi = 0^\circ$, $\theta_r = 0^\circ$ and $\psi = 0^\circ$, $\theta_r = 60^\circ$ at collision energies (a), (b) $E_{c.m.} = 96.96$ eV, (c), (d) 484.85 eV, (e), (f) 1454.55 eV, and (g), (h) 4848.48 eV. Electronically elastic, $n' = 0$ (brown lines); CT1, $n' = 1$ (blue lines); CT2, $n' = 2$ (green lines); CT3, $n' = 3$ (magenta lines).

$(X^3\Sigma_g^-) \rightarrow H^+ + O_2(X^3\Sigma_g^-)$] and for the CT channels $[H^+ + O_2(X^3\Sigma_g^-) \rightarrow H(^2S) + O_2^+(X^2\Pi_g)$ (CT1), $H(^2S) + O_2^+(a^4\Pi_u)$ (CT2), $H(^2S) + O_2^+(A^2\Pi_u)$ (CT3)]. It has been observed in the experiments of Gao *et al.* [8] that DCSs are strongly peaked in the forward directions ($\theta_{c.m.} \approx 0^\circ$), and they decay sharply with the increase in scattering angle. Therefore, a large fraction of the total cross section comes from the scattering angle below 1.0° .

It is worth noting that the DCS data often show oscillatory structures. Various reasons have been attributed to such

behavior. The electronic states, which correspond to the various excitation channels, interact among themselves. These interactions include Landau-Zener type (curve crossing, mostly in the small R -value range) [44]. Such interactions affect the transitions between the initial and final states of the system, and the scattering amplitudes corresponding to the different excitation pathways get affected due to such interactions, which is reflected in the DCS data. Structures may also arise due to the diffraction or rainbow scattering. These phenomena may also occur due to the interference effect in scattering arising from the attractive and repulsive parts of the potential surface(s), which however does not seem to be the case for forward scattering.

We have computed state-selected CT DCSs for $E_{c.m.} = 96.96$ and 1454.55 eV in order to investigate the charge transfer to the first (O_2^+ , $X^2\Pi_g$), the second (O_2^+ , $a^4\Pi_u$), and the third (O_2^+ , $A^2\Pi_u$) excited states. The plots for the respective DCSs are shown in Fig. 7. At $E_{c.m.} = 96.96$ eV, some structures are observed for scattering angle $\theta_{c.m.} = 1.0^\circ - 3.0^\circ$, followed by a decrease in the magnitude for all the CT channels. At $\theta_{c.m.} < 0.10^\circ$, the magnitude of CT2 is smaller by approximately an order of magnitude as compared to that of CT1. The magnitude of CT3 is smaller than that of CT2. For higher energy at $E_{c.m.} = 1454.55$ eV, the magnitudes for all CT channels increase, but the magnitude of the CT2 channel is approximately two orders of magnitude less as compared to the CT1 channel at $\theta_{c.m.} < 0.10^\circ$. Therefore, the comparison of their magnitudes for $E_{c.m.} = 96.96$ and 1454.55 eV, confirms our earlier analysis that, at relatively low collision energy, the probability of CT to higher excited states is higher than that at higher collision energy ranges. The excitation to the CT3 channel from the $H^+ + O_2(X^3\Sigma_g^-)$ is lower for both the collision energies. The CT1 channel $[H^+ + O_2(X^3\Sigma_g^-) \rightarrow H(^2S) + O_2^+(X^2\Pi_g)]$ is the most probable CT channel, as the total CT DCS lies close to that of the CT1 channel.

The plots for DCSs values for the electronically elastic process for collision energies $E_{c.m.} = 484.85$, 1454.55 , and 4848.48 eV are shown in the upper panel of Figs. 8(a)–8(c), respectively. Both the experimental and theoretical DCS data of Cabrera-Trujillo *et al.* [10] have also been reproduced there. Experimental data of Cabrera-Trujillo *et al.* [10] were carried out in scattering angle range of $0.15^\circ - 5.0^\circ$. Present calculated data show marginal overestimation of magnitude compared to DCS data of Cabrera-Trujillo *et al.* [10]. However, the overall behavior is predicted well in our calculations. We also observed oscillations in the DCS data which would be arising presumably due to the net effect of scattering from the various coupled electronic PESs.

In order to investigate further, we have computed DCSs for the most probable CT1 channel, $H^+ + O_2(X^3\Sigma_g^-) \rightarrow H(^2S) + O_2^+(X^2\Pi_g)$ at $E_{c.m.} = 484.85$, 1454.55 , and 4848.48 eV, and plotted them in the lower panel of Figs. 8(d)–8(f), respectively. Experimental data of Gao *et al.* [8] are reproduced in the same plot. Cabrera-Trujillo *et al.* [10] had a joint theoretical and experimental study, which are reproduced there. These studies reveal the existence of structures in the DCSs, which are also observed in our present calculations. Structures were observed at low collision energies in the experimental DCS data of Gao *et al.* [8], which is not so well

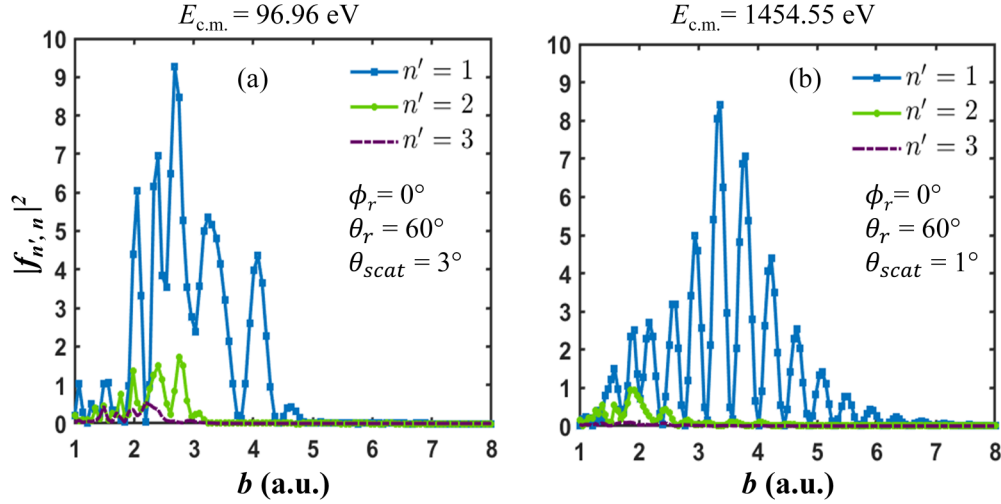


FIG. 6. Scattering amplitude $|f_{n',n}|^2$ [Eq. (11)] as a function of impact parameter b for molecular orientation $\phi_r = 0^\circ$, $\theta_r = 60^\circ$ at collision energies (a) $E_{c.m.} = 96.96$ eV and (b) 1454.55 eV. CT1, $n' = 1$ (blue lines); CT2, $n' = 2$ (green lines); CT3, $n' = 3$ (violet lines).

pronounced in the experiments of Cabrera-Trujillo *et al.* [10]. In our present calculation, structures are observed at relatively lower collision energy $E_{c.m.} = 484.85$ eV, and they tend to diminish at higher collision energies. As discussed earlier, the origin of these structures is presumably due to the accessibility and participation of higher CT channels at lower energies with relatively longer interaction time. It is important to note here that in the experiments of Gao *et al.* [8], the angular resolution was about 0.02° . Uncertainty in their data counts varied from 1% near $\theta_{lab} = 0.02^\circ$ to 10% near $\theta_{lab} = 1^\circ$. Accounting for these experimental uncertainties, the overall behavior of our computed data is in agreement with the earlier experimental observations.

Our paper involves the CT processes from the entrance channel $H^+ + O_2$ ($X^3\Sigma_g^-$) to the three CT channels O_2^+

($X^2\Pi_g$, $a^4\Pi_u$, $A^2\Pi_u$) with H^+ resulting in H (2S) after the electron transfer. At these high-energy collisions, still higher excited CT states could be possible, leading to H ($^2S^*$, 2P) states. Since the state-resolved CT DCS data could not be resolved in experiments, we believe the dynamics calculations, including other excited states of H and O_2^+ , may improve the results. A similar observation has also been noticed in the calculation of ICS data, which we discuss in the next section.

D. Integral cross sections

Integral cross sections for the CT process have been calculated both experimentally [8,11–16,45] and theoretically [10] in the collision energy range $E_{lab} = 0.01$ –100 keV. We have carried out integral cross-section calculations [Eq. (13)] for the CT process at $E_{c.m.} = 0.9696$ –9.696 keV ($E_{lab} = 0.1$ –10 keV), which are shown in Fig. 9 (green line). The early available experimental results of Stebbings *et al.* (red solid circles) [12], Gao *et al.* (black solid triangles) [8], Lindsay *et al.* (black solid stars) [45], and Cabrera-Trujillo *et al.* (dark cyan solid squares) [10] have been reproduced in the same plot in the stated collision range. Gao *et al.* [8] reported ICS values of 12, 9.5, and 9.0 \AA^2 in the laboratory frame at $E_{lab} = 0.5$, 1.0, and 1.5 keV. The ICS values reported by Stebbings *et al.* [12], Lindsay *et al.* [45], and Cabrera-Trujillo *et al.* [10] were nearly equal in magnitudes. The experimental error bars associated with the ICS data given by Cabrera-Trujillo *et al.* [10] are also shown in Fig. 9. The associated uncertainties were larger towards the lower collision energies. Our computed data show marginal underestimation as compared to the above-discussed experimental results. The earlier END calculations of Cabrera-Trujillo *et al.* [10] are based upon time-dependent variational principle, where wave functions are described as coherent state representations of the coupled electronic and nuclear wave functions; all energetically open CT channels were analyzed based on Mllikan’s population analysis of either the projectile or the target molecule. They reported ICSs by integrating the exchange DCSs over the scattering angles [see Eq. (7) of Ref. [10]] and by mapping

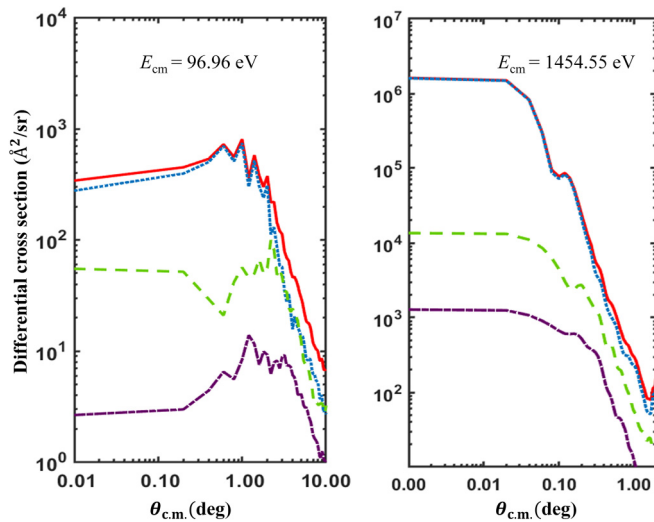


FIG. 7. State-selected DCSs for the CT processes of the $H^+ + O_2$ system as a function of scattering angle $\theta_{c.m.}$ for $E_{c.m.} = 96.96$ eV (left panel) and 1454.55 eV (right panel). Red solid lines represent total CT DCS, blue dotted lines represent CT1, green dashed lines represent CT2, and magenta dot-dashed lines represent CT3.

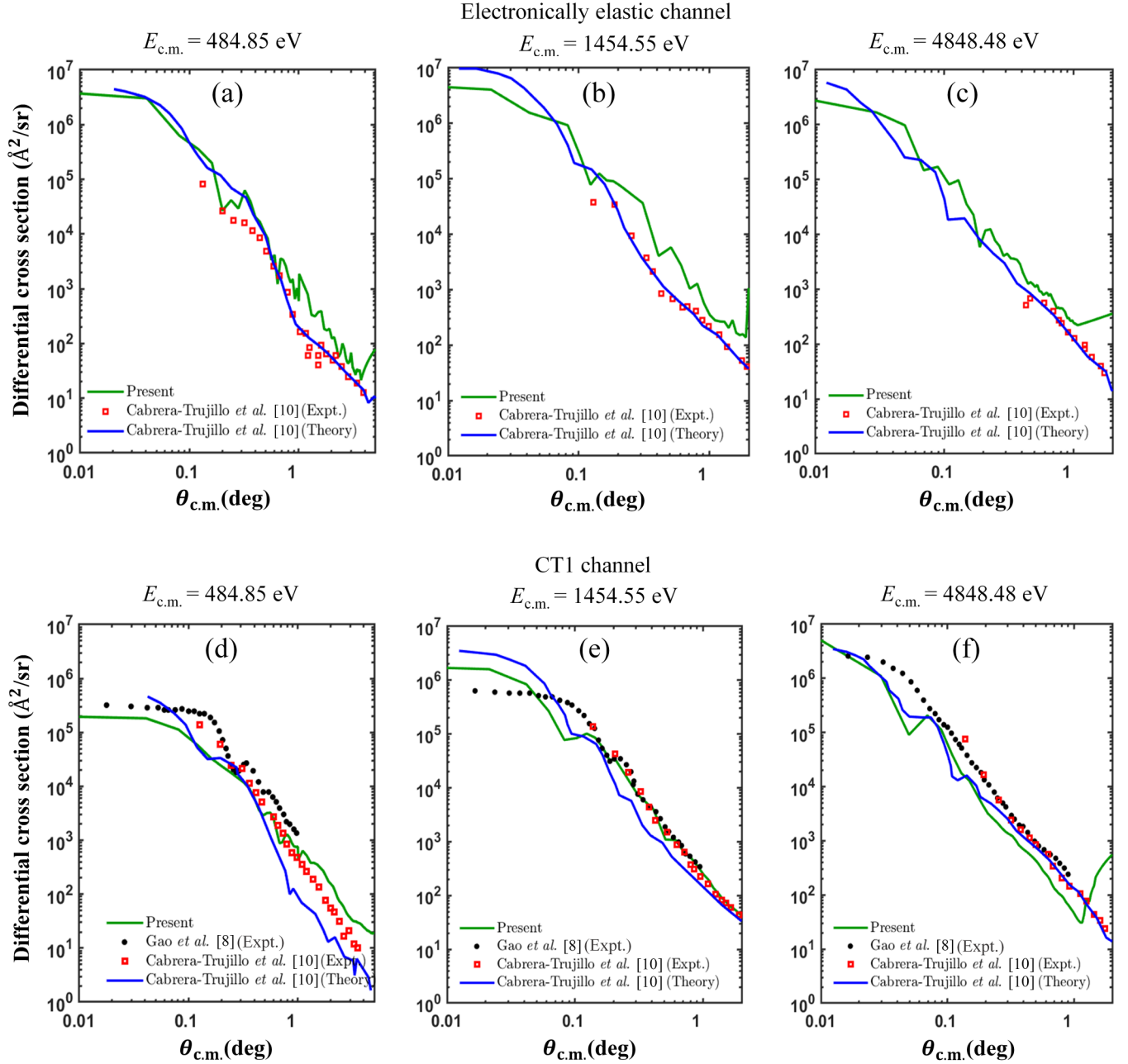


FIG. 8. DCSs for the electronically elastic (a)–(c) and CT1 (d)–(f) processes of the $\text{H}^+ + \text{O}_2$ system as a function of scattering angle, $\theta_{\text{c.m.}}$. Green lines represent our computed results; black solid circles represent experimental results of Gao *et al.* [8]; red squares represent experimental data of Cabrera-Trujillo *et al.* [10]; blue lines represent theoretical results of Cabrera-Trujillo *et al.* [10].

the impact parameter (b) [see Eq. (8) of Ref. [10]] which have been shown in Fig. 9 (as blue dash and pink solid line, respectively). They also obtained the total CT leading to the hydrogen atom in the 2S state by projecting the total electronic wave function onto the $1s$ state of hydrogen, which is shown in Fig. 9 (violet double dash line). Our calculated ICS data (green line) are nearly equal in magnitude as compared to the ICS data of Cabrera-Trujillo *et al.* [10] (violet double dash line) in the studied collision energy range. As discussed in the preceding section, the present CT calculations are performed on the electronic states asymptotically correlating to $\text{H}(^2S) + \text{O}_2^+(X^2\Pi_g)$ (CT1), $\text{H}(^2S) + \text{O}_2^+(a^4\Pi_u)$ (CT2), and $\text{H}(^2S)$

+ $\text{O}_2^+(A^2\Pi_u)$ (CT3) channels. Thus, we have taken into consideration the 2S state of H in our calculations, which leads to an almost similar observation as reported by Cabrera-Trujillo *et al.* [10] (violet double dash line). However, electron capture into the $2s$ and $2p$ states of H may also contribute to the total CT process for the system. We believe that the inclusion of CT states leading to excited states of H ($^2S^*$, 2P) will improve the overall ICS magnitude. In the present calculations, we have used the potential couplings among the four electronic states evaluated at $r = r_e = 2.293$ a.u. of the ground electronic state of O_2 . Although the straight line trajectory assumption of the projectile is largely justified in the high-energy collision

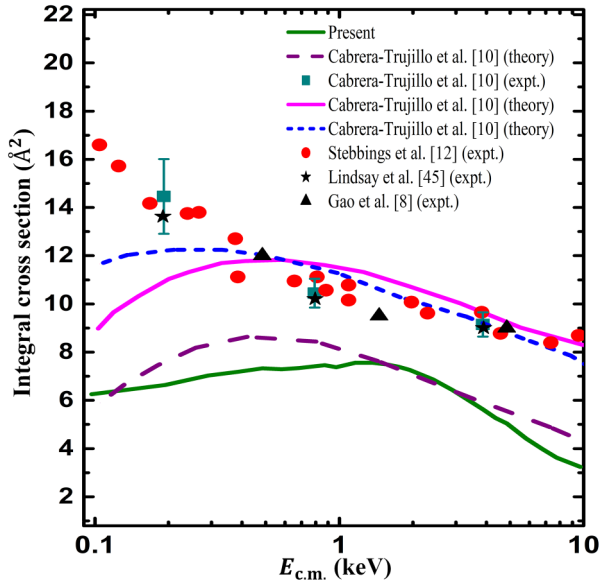


FIG. 9. Charge-transfer ICSs as a function of collision energy $E_{c.m.}$ of the $H^+ + O_2$ system. Green line represents our computed integral cross sections; red solid circles represent experimental data of Stebbings *et al.* [12]; black solid stars represent experimental results of Lindsay *et al.* [45]; black solid triangles represent experimental ICSs of Gao *et al.* [8]; dark cyan solid squares represent experimental results of Cabrera-Trujillo *et al.* [10]; lines (pink solid, blue dash, and violet double dash) represent theoretical data of Cabrera-Trujillo *et al.* [10].

regimes, the variance with the experiments can be improved further by considering the following: (i) the vibrationally averaged electronic potentials and couplings to include the vibrational component and its effect and (ii) inclusion of further higher energetically opened charge-transfer states in the calculations since the details of the involved CT states are not available from the experiments and they could provide only the total CT differential cross sections.

V. SUMMARY AND CONCLUSION

We have performed high-energy collision dynamics for the CT processes in the $H^+ + O_2$ system within the semiclassical straight line trajectory approach for the forward scattering for collision energies $E_{c.m.} = 0.096\text{--}4.848$ keV. The dynamics has been performed on *ab initio* rigid-rotor quasidiabatic PESs on the four lowest electronic states correlating to $H^+ + O_2$ ($X^3\Sigma_g^-$) (electronically elastic), $H(^2S) + O_2^+(X^2\Pi_g)$ (CT1), $H(^2S) + O_2^+(a^4\Pi_u)$ (CT2), and $H(^2S) + O_2^+(A^2\Pi_u)$ (CT3). The analysis of behavior and magnitudes of NACME values (τ^1) suggest that CT1 is the most probable CT process. The CT2 and CT3 processes could become probable only at lower collision energies ($E_{c.m.} \approx 100$ eV) through indirect flux transfer from CT1 to CT2 and from CT2 to CT3, as the projectile (H^+) spends a longer duration near the target (O_2). This is reflected in the calculated dynamical attributes such as DCSs and ICSs. Oscillations in DCSs are observed, which are more pronounced at lower energies than at higher energies. This could be arising due to the larger participation of high CT states at lower energies. The computed DCSs and ICSs for the electronically elastic and the charge-transfer processes are found to be in good agreement with early experimental and theoretical outcomes, lending credence to the accuracy of the quasidiabatic PESs obtained and to the adequacy of the quasidiabatization procedure based on the *ab initio* approach.

However, we have observed some discrepancies in the DCSs and ICSs data, which can be further improved through the inclusion of higher excited states. An improvement can also be achieved in the present semiclassical calculations by considering the vibrational-electronic couplings, especially towards the low collision energy ranges.

ACKNOWLEDGMENTS

We acknowledge High Performance Computing Environment of Indian Institute of Technology Madras for the computing facilities. D.R. is also thankful for scholarship support from Indian Institute of Technology Madras.

- [1] M. Larsson, W. Geppert, and G. Nyman, *Rep. Prog. Phys.* **75**, 066901 (2012).
- [2] M. E. Rudd, T. V. Goffe, A. Itoh, and R. D. DuBois, *Phys. Rev. A* **32**, 829 (1985).
- [3] D. Bodewits, R. Hoekstra, B. Seredyuk, R. McCullough, G. Jones, and A. Tielens, *Astrophys. J.* **642**, 593 (2006).
- [4] T. Kusakabe, S. Kitamuro, Y. Nakai, H. Tawara, and M. Sasao, *Plasma Fusion Res.* **7**, 2401062 (2012).
- [5] G. Niedner-Schatteburg and J. P. Toennies, in *Advances in Chemical Physics*, edited by C.-Y. Ng, M. Baer, I. Prigogine, and S. A. Rice (Wiley Online Library, New York, 1992), Vol. 82, pp. 553–646.
- [6] F. Gianturco, U. Gierz, and J. P. Toennies, *J. Phys. B* **14**, 667 (1981).
- [7] S. Amaran and S. Kumar, *J. Chem. Sci.* **121**, 797 (2009).
- [8] R. S. Gao, L. K. Johnson, C. L. Hakes, K. A. Smith, and R. F. Stebbings, *Phys. Rev. A* **41**, 5929 (1990).
- [9] J. Newman, K. Smith, R. Stebbings, and Y. Chen, *J. Geophys. Res.: Space Phys.* **90**, 11045 (1985).
- [10] R. Cabrera-Trujillo, Y. Öhrn, E. Deumens, J. R. Sabin, and B. G. Lindsay, *Phys. Rev. A* **70**, 042705 (2004).
- [11] P. M. Stier and C. Barnett, *Phys. Rev.* **103**, 896 (1956).
- [12] R. Stebbings, A. Smith, and H. Ehrhardt, *J. Geophys. Res.* **69**, 2349 (1964).
- [13] H. H. Fleischmann, R. A. Young, and J. W. McGowan, *Phys. Rev.* **153**, 19 (1967).
- [14] D. W. Koopman, *Phys. Rev.* **166**, 57 (1968).
- [15] B. Siegmann, U. Werner, Z. Kaliman, Z. Roller-Lutz, N. M. Kabachnik, and H. O. Lutz, *Phys. Rev. A* **66**, 052701 (2002).
- [16] J. López-Patiño, B. Fuentes, F. B. Yousif, and H. Martínez, *Int. J. Mass Spectrom.* **405**, 59 (2016).
- [17] Y. Öhrn, E. Deumens, A. Diz, R. Longo, J. Oreiro, and H. Taylor, *Time-Dependent Quantum Molecular Dynamics* (Plenum, New York, 1992).

- [18] R. Longo, E. Deumens, and Y. Öhrn, *J. Chem. Phys.* **99**, 4554 (1993).
- [19] T. H. Dunning, Jr., *J. Chem. Phys.* **90**, 1007 (1989).
- [20] G. J. Vazquez, R. J. Buenker, and S. D. Peyerimhoff, *Mol. Phys.* **59**, 291 (1986).
- [21] F. Schneider, L. Zülicke, F. DiGiacomo, F. Gianturco, I. Paidarová, and R. Polák, *Chem. Phys.* **128**, 311 (1988).
- [22] D. Grimbert, B. Lassier-Govers, and V. Sidis, *Chem. Phys.* **124**, 187 (1988).
- [23] F. Gianturco, A. Palma, and F. Schneider, *Int. J. Quantum Chem.* **37**, 729 (1990).
- [24] S. Amaran and S. Kumar, *J. Chem. Phys.* **128**, 154325 (2008).
- [25] V. Saheer and S. Kumar, *J. Chem. Sci.* **130**, 149 (2018).
- [26] M. Sizun, D. Grimbert, V. Sidis, and M. Baer, *J. Chem. Phys.* **96**, 307 (1992).
- [27] M. Noll and J. P. Toennies, *J. Chem. Phys.* **85**, 3313 (1986).
- [28] D. Simah, B. Hartke, and H.-J. Werner, *J. Chem. Phys.* **111**, 4523 (1999).
- [29] R. Schinke, *Chem. Phys.* **24**, 379 (1977).
- [30] R. Schinke, H. Krüger, V. Hermann, H. Schmidt, and F. Linder, *J. Chem. Phys.* **67**, 1187 (1977).
- [31] M. Baer and C.-Y. Ng, *State-Selected and State-to-State Ion-Molecule Reaction Dynamics*, Part 2, Theory (Wiley Online Library, New York, 1992).
- [32] A. Lebehot and R. Campargue, *J. Phys. B* **15**, 1711 (1982).
- [33] J. C. Tully, *Dynamics of Molecular Collisions: Part B* (Springer, New York, 1976), pp. 217–267.
- [34] V. Sidis, *Collision Theory for Atoms and Molecules* (Springer, New York, 1989), pp. 343–400.
- [35] V. Sidis, in *Advances in Atomic, Molecular, and Optical Physics* (Elsevier, New York, 1989), Vol. 26, pp. 161–208.
- [36] E. Gislason and D. Herschbach, *J. Chem. Phys.* **64**, 2133 (1976).
- [37] G. N. Watson, *A Treatise on the Theory of Bessel Functions* (The University Press, Cambridge, 1922).
- [38] M. Wartell and R. Cross, Jr., *J. Chem. Phys.* **55**, 4983 (1971).
- [39] H. Krüger and R. Schinke, *J. Chem. Phys.* **66**, 5087 (1977).
- [40] See Supplemental Material at <http://link.aps.org/supplemental/10.1103/PhysRevA.110.032802> for the *ab initio* PESs and potential couplings data points.
- [41] H. Werner, P. Knowles, G. Knizia, F. Manby, M. Schütz, P. Celani, T. Korona, R. Lindh, A. Mitrushenkov, G. Rauhut *et al.*, *Chem. Phys.* **152**, 144107 (2020).
- [42] C. A. Mead and D. G. Truhlar, *J. Chem. Phys.* **70**, 2284 (1979).
- [43] S. Faraji, S. Matsika, and A. I. Krylov, *J. Chem. Phys.* **148**, 044103 (2018).
- [44] L. D. Landau, *Phys. Z. Sowjetunion* **2**, 46 (1932).
- [45] B. G. Lindsay, D. R. Sieglaff, D. A. Schafer, C. L. Hakes, K. A. Smith, and R. F. Stebbings, *Phys. Rev. A* **53**, 212 (1996).